

# Surface recombination velocity imaging of wet-cleaned silicon wafers using quantitative heterodyne lock-in carrierography

Cite as: Appl. Phys. Lett. **112**, 012105 (2018); <https://doi.org/10.1063/1.5003260>

Submitted: 04 September 2017 . Accepted: 16 December 2017 . Published Online: 04 January 2018

 Qiming Sun, Alexander Melnikov, Andreas Mandelis, and  Robert H. Pagliaro

## COLLECTIONS

 This paper was selected as an Editor's Pick



View Online



Export Citation



CrossMark

## ARTICLES YOU MAY BE INTERESTED IN

[Quantitative self-calibrating lock-in carrierographic lifetime imaging of silicon wafers](#)

Applied Physics Letters **101**, 242107 (2012); <https://doi.org/10.1063/1.4772207>

[Uniqueness range optimization of photocarrier transport parameter measurements using combined quantitative heterodyne lock-in carrierography imaging and photocarrier radiometry](#)

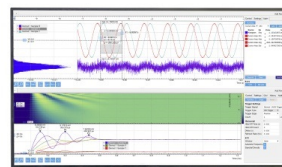
Journal of Applied Physics **125**, 065701 (2019); <https://doi.org/10.1063/1.5083168>

[Infrared lock-in carrierography \(photocarrier radiometric imaging\) of Si solar cells](#)

Journal of Applied Physics **107**, 114513 (2010); <https://doi.org/10.1063/1.3407521>

Challenge us.

What are your needs for periodic signal detection?



Zurich Instruments



## Surface recombination velocity imaging of wet-cleaned silicon wafers using quantitative heterodyne lock-in carrierography

Qiming Sun,<sup>1,2</sup> Alexander Melnikov,<sup>1</sup> Andreas Mandelis,<sup>1,2,3,a)</sup> and Robert H. Pagliaro<sup>4</sup>

<sup>1</sup>*Center for Advanced Diffusion-Wave and Photoacoustic Technologies (CADIPT), University of Toronto, Toronto, Ontario M5S 3G8, Canada*

<sup>2</sup>*School of Optoelectronic Information, University of Electronic Science and Technology of China, Chengdu 610054, China*

<sup>3</sup>*Diffusion-Wave Diagnostic Technologies, Toronto, Ontario M1M 2V3, Canada*

<sup>4</sup>*Advanced Processing Equipment Technology (APET) Co., Ltd, 20-15, Sukwoo-Dong, Hwaseong-City, Gyeonggi-do 463-802, South Korea*

(Received 4 September 2017; accepted 16 December 2017; published online 4 January 2018)

InGaAs-camera based heterodyne lock-in carrierography (HeLIC) is developed for surface recombination velocity (SRV) imaging characterization of bare (oxide-free) hydrogen passivated Si wafer surfaces. Samples prepared using four different hydrofluoric special-solution etching conditions were tested, and a quantitative assessment of their surface quality vs. queue-time after the hydrogen passivation process was made. The data acquisition time for an SRV image was about 3 min. A “round-trip” frequency-scan mode was introduced to minimize the effects of signal transients on data self-consistency. Simultaneous best fitting of HeLIC amplitude-frequency dependencies at various queue-times was used to guarantee the reliability of resolving surface and bulk carrier recombination/transport properties. The dynamic range of the measured SRV values was established from 0.1 to 100 m/s. *Published by AIP Publishing.* <https://doi.org/10.1063/1.5003260>

Surface preparation has become amongst the most important fabrication steps in the electronic device manufacturing industry. Leading edge semiconductor devices require methods to provide stable, pristine, “oxide free,” and hydrogen passivated silicon surfaces to accommodate low thermal budget requirements for other critical processes like epitaxy, CVD, ion implantation, and gate oxidation. This can be achieved using wet cleaning process chemistries such as diluted hydrofluoric (HF) acid to maximize the hydrogen termination efficiency and to minimize surface contaminants and micro-roughness.<sup>1,2</sup> One of the key issues surface preparation experts are facing has been the ability to quantify the integrity of the dynamically changing surface conditions that come with creating bare silicon surfaces. The surface of bare silicon wafers changes in air with exposure time (“queue-time” or “Q-time”) due to native oxide growth.<sup>3</sup> The ability to suppress this naturally occurring phenomenon is also a key goal of the surface preparation process.

Carrier recombination and transport properties such as the effective carrier lifetime, the carrier diffusion length, and the surface recombination velocity (SRV) are parameters very sensitive to impurity/defect densities even at room temperature, thus being routinely measured in the IC industry as a process cleanliness monitor.<sup>4</sup> For “as processed” silicon surfaces, quantitative characterization of the SRV and/or the effective lifetime are ideal since they capture everything that can produce a negative impact on the surface quality of the wafer. The culprits include metals, organics, oxygen, other unintentional impurities, and micro-roughness.

PhotocARRIER Radiometry (PCR),<sup>5</sup> an all-optical (contactless), dynamic (frequency-domain), spectrally gated, and

diffusion-wave-based photoluminescence (PL) characterization technique, has been demonstrated to be capable of quantitatively characterizing bulk, surface, interface, junction, and trap-state properties of various semiconductor materials and devices.<sup>6–10</sup> Lock-in carrierography (LIC),<sup>11</sup> an imaging extension of PCR, has been developed to provide both spatially resolved<sup>12</sup> and globally integrated<sup>13,14</sup> information of materials and devices. Recently, a heterodyne mode of LIC (HeLIC) was introduced to overcome the speed limitations (frame rate and exposure time) of InGaAs cameras and realize high-frequency imaging, which allows ~100-Hz-limited infrared cameras to monitor microsecond physical processes.<sup>15–17</sup>

In this paper, we demonstrate a study undertaken to evaluate the HeLIC characterization method for measuring a matrix of five “as processed” bare Si wafers using quantitative HeLIC characterization of HF-etched wafers through SRV imaging. In principle, both the SRV and the effective lifetime are available parameters for assessing “oxide free” surface preparation processes;<sup>18,19</sup> however, in this investigation, we chose the SRV to be the parameter for quantitative characterization as it is most closely related to surface changes. The concept of effective lifetime is simple to understand but not quantitatively rigorous. It is a highly averaged (both spatially and temporally) parameter so that different measurement methods may yield widely differing effective lifetimes for the same material or device, mainly due to different weighing among techniques, not due to a deficiency of the technique(s).<sup>3,19–21</sup> In contrast, SRV is a more specific and physically meaningful parameter, rigorously defined by the third kind boundary condition in the carrier diffusion field boundary value problem,<sup>22</sup> and so, there is no “excuse” for different techniques to yield different SRVs from the same sample.

<sup>a)</sup> Author to whom correspondence should be addressed: mandelis@mie.utoronto.ca

The samples under test were p-type float-zone (FZ) wafers with resistivity  $\geq 10 \text{ k}\Omega \text{ cm}$ , 150-mm in diameter, and 675- $\mu\text{m}$  thick. Sample No. 1 was processed using a TeraDox<sup>TM</sup> instrument developed by Advanced Processing Equipment Technology (APET),<sup>23</sup> featuring 100:1 HF with a 40-ppb dissolved oxygen (DO) level; No. 2 was processed with the same system using 100:1 HF with a 400-ppb DO level; No. 3 was processed with a multi-vessel wet bench system using 100:1 HF with a 2-ppm DO level (not degassed); No. 4 was etched with the University of Toronto's in-house wet bench using 2% HF (not degassed); and No. 5 had undergone no etching/cleaning process and was used as a control sample.

A schematic of the experimental HeLIC system can be found in Ref. 16. Briefly, for optical excitation in our experiments, two beams of 808-nm fiber-coupled lasers were collimated, then spread, and homogenized by micro-lens arrays to form a  $5 \times 5 \text{ cm}^2$  illuminated area. The light was square-wave modulated (3-W average power for each at the output end) by a two-channel function generator, with the frequency difference between the two channels fixed at 2 Hz, which was also the frequency of the lock-in reference signal generated by a data acquisition card. An InGaAs camera was used with  $320 \times 256$  pixels, a 0.9–1.7- $\mu\text{m}$  spectral range, a 16.6-ms exposure time (i.e., the single-frame capture integration time of the camera), and a 60-Hz frame rate, and so, 30 images could be captured within a 2-Hz lock-in period. To improve the signal-to-noise ratio, 25-period signals were accumulated and averaged for the lock-in calculation. With this configuration, the data acquisition time for one HeLIC amplitude image was 12.5 s.

By virtue of the heterodyne mode, there is no upper frequency limit for lock-in imaging, and so, one can freely choose appropriate frequency ranges and the number of frequency points according to specific samples under test. In view of the diffusive nature of carrier density waves,<sup>5,22</sup> the frequency scan range should be chosen to cover the “knee” frequency point  $\omega\tau_e \sim 1$  (Ref. 11) in order to guarantee the sensitivity of PCR/LIC signals to the carrier recombination parameters, where  $\omega$  is the angular modulation frequency and  $\tau_e$  is the effective lifetime. Based on this principle, the frequency range for sample No. 1 in the test was chosen to be from 100 Hz to 1 kHz, as its  $\tau_e$  at early Q-times was roughly estimated to be on the order of 1 ms, while all other samples were tested from 100 Hz to 10 kHz.

Our preliminary tests of HF-etched Si wafers showed that PCR/LIC signals were not stable and changing with time. This may originate from both the natural evolution of surface quality degradation due to native oxide growth in air<sup>1–3</sup> and the interaction between laser irradiation and the semiconductor surface.<sup>24</sup> Detailed investigation of this phenomenon is out of the scope of this paper. A method to minimize the influence of the laser-surface interaction effects on HeLIC signal transients self-consistently with respect to the amplitude frequency dependence was to run the scans in a “round-trip” mode: we scanned the frequency from low to high and then back. Fig. 1 shows the general behavior of the round-trip HeLIC amplitude vs. frequency experimental data from an arbitrary camera pixel. In order to guarantee the data reliability, we reduced the  $f$ -scan points to 11 so as to shorten the measurement time and always used the average of the

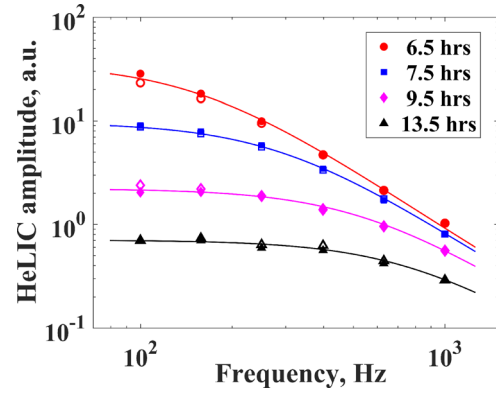


FIG. 1. HeLIC amplitude-frequency dependencies of sample No. 1 in terms of a camera pixel signal evolution at four Q-times. The “round-trip” information is shown as solid symbols (forward) and hollow symbols (reverse) for frequency scans. The actual dependence used for quantitative analysis is their average. The solid curves are the corresponding theoretical best fits.

forward and the reverse frequency-scan data as the final dependence for quantitative analysis.

A theoretical model was used to extract the SRV values from the experimental HeLIC amplitude-frequency data. The excess carrier density wave generated by spread and homogenized laser beams was determined by the one-dimensional partial differential carrier diffusion equation subject to a harmonic source and third kind boundary conditions

$$\begin{cases} D \frac{\partial^2 n}{\partial z^2} - \frac{n}{\tau_b} - \frac{\partial n}{\partial t} = -G_0 \beta e^{-\beta z} g(t) \\ D \frac{\partial n(t, z)}{\partial z} \Big|_{z=0} = sn(t, 0) \\ D \frac{\partial n(t, z)}{\partial z} \Big|_{z=L} = -sn(t, L), \end{cases} \quad (1)$$

where  $D$  is the carrier ambipolar diffusivity,  $\tau_b$  the bulk lifetime,  $G_0$  the average optical generation rate,  $\beta$  the optical absorption coefficient,  $g(t)$  the modulation function,  $L$  the sample thickness, and  $s$  the SRV. Here, a symmetrical case of the sample with respect to the front and the back surfaces was assumed. The frequency-domain solution  $n(\omega, z)$  of Eq. (1) can be expressed as

$$n(\omega, z) = C_1 e^{-\sigma z} + C_2 e^{-\sigma(L-z)} - \frac{G_0 \beta}{D(\beta^2 - \sigma^2)} e^{-\beta z}, \quad (2)$$

with  $\sigma = [(\tau_b^{-1} + i\omega)/D]^{1/2}$  and

$$\begin{cases} C_1 = \frac{G_0 \beta [(D\sigma + s)(D\beta + s) - (D\sigma - s)(D\beta - s)e^{-(\sigma+\beta)L}]}{D(\beta^2 - \sigma^2) [(D\sigma + s)^2 - (D\sigma - s)^2 e^{-2\sigma L}]} \\ C_2 = \frac{G_0 \beta [(D\sigma - s)(D\beta + s)e^{-\sigma L} - (D\sigma + s)(D\beta - s)e^{-\beta L}]}{D(\beta^2 - \sigma^2) [(D\sigma + s)^2 - (D\sigma - s)^2 e^{-2\sigma L}]} \end{cases} \quad (3)$$

The HeLIC signal can be expressed in the form<sup>16</sup>

$$S(\Delta\omega) = C \int_0^L n(-\omega_1, z) n(\omega_2, z) dz, \quad (4)$$

where  $\Delta\omega = \omega_2 - \omega_1$  (always set at 2 Hz in the reported experiments) and  $C$  is a proportionality factor. Here,  $n(-\omega_1, z) = n^*(\omega_1, z)$  indicates the nonlinear frequency mixing and the beat-frequency detection nature of heterodyne signals, where  $*$  denotes the complex conjugation.

The proportionality factor  $C$  in Eq. (4) takes all the proportionality factors into account, such as the band-to-band carrier radiative recombination coefficient, the surface reflectivity of samples with respect to the near-infrared PL, the PL detection solid angle, the optoelectronic conversion efficiency of the InGaAs-camera detector matrix, and the digitized camera-to-computer outputs. During the best fitting of Eq. (4) to the HeLIC amplitude vs. frequency data, the proportionality factor  $C$  acts as a normalizing constant, which scales the theoretical curves in order to draw the experimental data and the theoretical curves together for comparison. The proportionality factor  $C$  has no influence on the best fitting outputs, as after normalization, the shape of the amplitude vs. frequency data curve (dynamic behavior) is the only criterion to judge which theoretical curve is the best fit.

The parameters that influence the dynamic behavior of Eq. (4) are  $\beta$  ( $=789 \text{ cm}^{-1}$  at 808 nm),  $\tau_b$ ,  $D$ , and  $s$ . Due to the compromised number of data points, there may be a non-uniqueness problem if all the aforementioned parameters are set as free parameters during multi-parameter fitting. Therefore, two assumptions were made: (1) in view of the fact that the substrates of the five samples under test were high-resistivity FZ c-Si, the carrier diffusivity value was assumed to be  $18 \text{ cm}^2/\text{s}$  (the ambipolar diffusivity),<sup>22,25</sup> and so, the two remaining free parameters for each data set were the bulk lifetime and the SRV; and (2) the HeLIC  $f$ -scan data at different Q-times, shown in Fig. 1, were simultaneously fitted, assuming that the bulk lifetime does not change, and

the only factor that makes the four data curves different is the degrading SRV. These restrictions can highly improve fitting uniqueness and reliability. The theoretical best fits to the data shown in Fig. 1 are also presented as solid curves; the corresponding extracted four SRV and one bulk lifetime values are 0.31 m/s, 0.62 m/s, 1.25 m/s, 1.89 m/s, and 9.23 ms, respectively.

By best fitting the  $f$ -scan data at all image pixels, quantitative images can be obtained as shown in Fig. 2. The HeLIC amplitude image of sample No. 1 at 100 Hz ( $f_2 = 102 \text{ Hz}$ ) is shown in Fig. 2(a) as an example; in fact, 11 HeLIC amplitude images at different frequencies were needed to reconstruct each SRV image. Although there exist plenty of image processing software to improve image quality, the image shown in Fig. 2(a) is the raw data from the camera, without any post-processing such as uniformity correction. The reasons that we did not introduce image post-processing are (1) to keep the original pixel responses in order not to distort the signal transients artificially; and (2) HeLIC is a dynamic imaging methodology, whose quantitative capability relies on how the amplitude changes with frequency, not relying on a single amplitude absolute value, and so, in principle, no calibration is needed even in the presence of instrumentation-induced amplitude level inhomogeneity.<sup>12</sup>

The SRV images of sample No. 1 at three different Q-times are shown in Figs. 2(b)–2(d), sequentially. It can be seen that at a Q-time of 6.5 h, the SRV of sample No. 1 was basically ranging from 0.23 to 0.3 m/s; it gradually increased vs. Q-time, as the thickness of the oxide layer grew gradually on the sample surfaces; at a Q-time of 9.5 h, the SRV value reached ca. 1.1 m/s. The trend of the natural evolution of SRV vs. Q-time can be clearly seen from the statistical distributions of the number of pixels shown in Fig. 2(e). As a

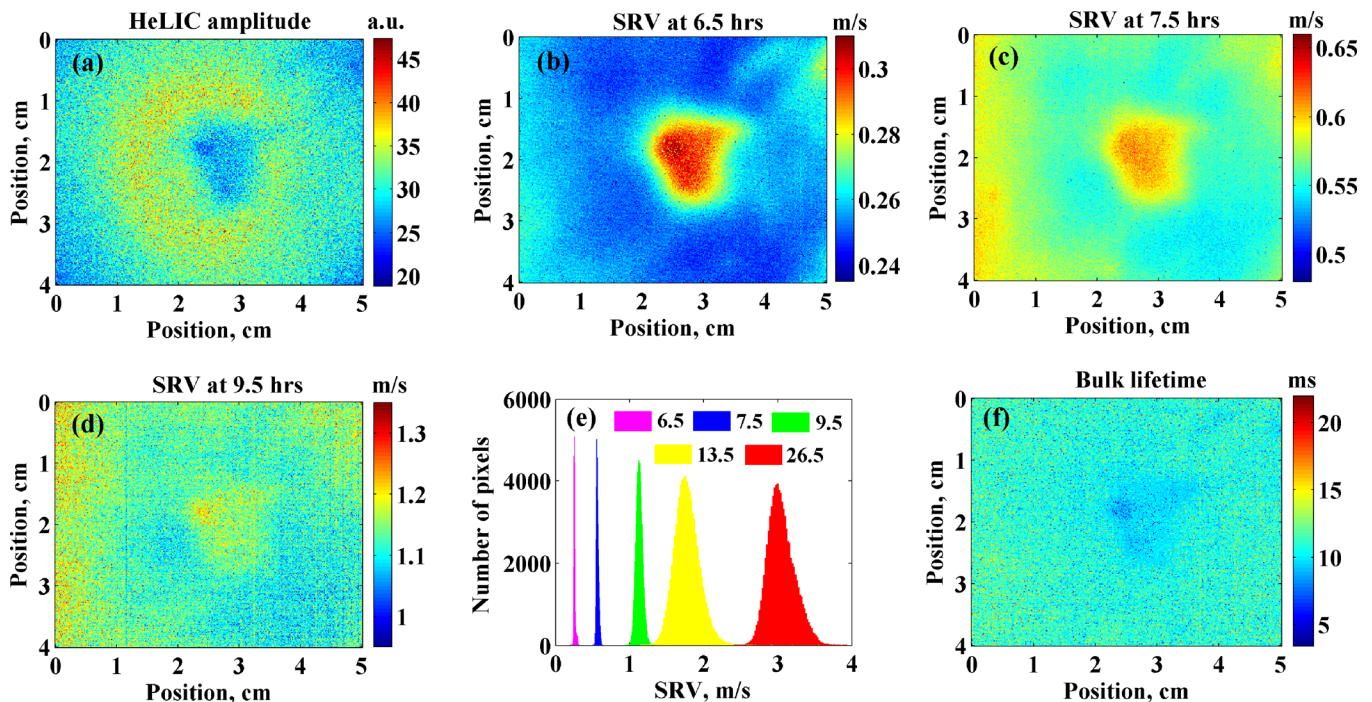


FIG. 2. Imaging results of sample No. 1. (a) HeLIC amplitude image at 100 Hz (raw image, no uniformity or smooth correction); (b)–(d) SRV images at various Q-times; (e) pixel-value statistical distributions of SRV images at various Q-times (hours); and (f) bulk lifetime image.

by-product, the bulk lifetime image was also obtained and is shown in Fig. 2(f), from which one can see that the bulk lifetime of this FZ wafer is on the order of 10 ms.

The averaged values over a whole SRV image at different Q-times can reflect the global behavior of the sample. Figure 3 shows the comparison of the image-averaged SRV values among the five samples. The control sample (No. 5) has an average SRV value of 67.7 m/s, while the remaining four samples feature much lower SRV values, indicating that the electronic surface states were highly passivated after the surface treatments with HF.<sup>18,26</sup> Among sample Nos. 1–3, sample No. 1 has the lowest SRV, as expected, due to the lowest DO level; the sample with in-house prepared dilute HF etching (No. 4) has an average SRV value of 3.6 m/s during the first measurement. By comparing the results of the advanced cleaning solution (Nos. 1–3) with those of the in-house cleaning solution (No. 4), one can observe a general trend with the curves of Nos. 1–3 shifted to the right on the time axis compared to that of No. 4. This indicates that the advanced cleaning solution significantly impedes the appearance of surface trap states (delays on the order of 10h) before oxidation after which surface state regeneration reaches the level of those attained with the in-house cleaning solution.

Although further study is needed in order to obtain a deeper insight into the physics/chemistry involved in the evolution (natural and/or artificial) of the sample surface quality (especially at very early times after etching), for the results shown in this report, it is clear that the influence of the laser irradiation on the SRV results was not the dominant factor compared to the natural behavior, as the SRV values of the 5 samples having undergone 4 different etching processes but the same laser irradiation were well distinguished, and the comparison of their SRV values was as expected.

Other improvements in HeLIC imaging of dynamic SRV evolution can be made in at least two fronts: (1) by implementing higher-power lasers, the imaged area can be extended from the present  $5 \times 4 \text{ cm}^2$  area to the entire wafer in order to achieve truly global real-time characterization; and (2) imaging time can be further reduced by introducing *waveform engineering*<sup>27</sup> such as frequency chirping in order to be able to better accommodate the requirement for industrial fast in-line quality control.

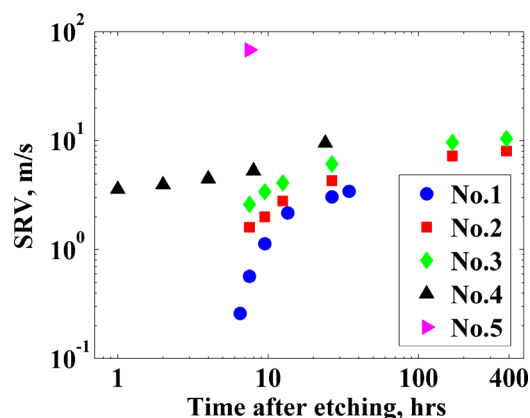


FIG. 3. Comparison of image-averaged SRV values among the five samples.

In conclusion, HeLIC has been demonstrated to be able to provide quantitative imaging characterization of surface quality of bare “oxide-free” hydrogen passivated Si wafers. Compared to other popular semiconductor characterization techniques such as microwave photoconductivity decay, steady-state and quasi-steady-state PL, surface charge analyzer, and surface photovoltage, LIC is the only technique that features all the following merits/advantages together: (1) being all-optical and noncontact, it is truly nondestructive and promising for fast in-line inspection; (2) imaging, instead of single-point detection, can provide both spatially resolved and globally integrated information of semiconductor substrates and devices; (3) camera based, it needs only minutes to produce a quantitative image with a full camera pixel resolution, much faster than point-by-point scan lifetime imaging techniques; (4) dynamic and calibration free, compared to steady-state PL imaging,<sup>28,29</sup> HeLIC quantitative capability relies on the dynamic behavior of amplitude vs. frequency dependence, not on a single camera-pixel absolute value; (5) with separation capability of bulk and surface properties by virtue of the depth-selective nature of diffusion-wave based techniques;<sup>22</sup> and (6) with its high-frequency imaging ability ( $\omega\tau_c \gg 1$ ) by virtue of the heterodyne lock-in mode, HeLIC allows millisecond to sub-microsecond physical processes to be accessed dynamically through today’s much slower (100-Hz) frame-rate cameras.

The authors are grateful to NSERC for a Discovery grant, to CFI for equipment grants, to the Canada Research Chairs Program, and to the Lawrence Semiconductor Research Laboratory for their wafer donation. Q.M.S. acknowledges the NNSFC (Grant Nos. 61601092 and 61771103).

<sup>1</sup>M. Morita, T. Ohmi, E. Hasegawa, M. Kawakami, and K. Suma, *Appl. Phys. Lett.* **55**, 562 (1989).

<sup>2</sup>F. H. Li, M. K. Balazs, and S. Anderson, *J. Electrochem. Soc.* **152**, G669 (2005).

<sup>3</sup>P. Brabant, J. Ferrara, B. Pagliaro, K. Weeks, M. Rittgers, R. Scott, Y. Zhang, T. Landin, T. Irving, J. Spear, J. Italiano, and S. G. Thomas, *Appl. Surf. Sci.* **255**, 1741 (2008).

<sup>4</sup>D. K. Schroder, *Semiconductor Material and Device Characterization*, 3rd ed. (John Wiley & Sons, 2015), p. 389.

<sup>5</sup>A. Mandelis, J. Batista, and D. Shaughnessy, *Phys. Rev. B* **67**, 205208 (2003).

<sup>6</sup>J. Batista, A. Mandelis, and D. Shaughnessy, *Appl. Phys. Lett.* **82**, 4077 (2003).

<sup>7</sup>D. Shaughnessy, B. C. Li, A. Mandelis, and J. Batista, *Appl. Phys. Lett.* **84**, 5219 (2004).

<sup>8</sup>B. C. Li, D. Shaughnessy, A. Mandelis, J. Batista, and J. Garcia, *J. Appl. Phys.* **95**, 7832 (2004).

<sup>9</sup>A. Melnikov, A. Mandelis, B. Halliop, and N. P. Kherani, *J. Appl. Phys.* **114**, 244506 (2013).

<sup>10</sup>Y. C. Zhang, A. Melnikov, A. Mandelis, B. Halliop, N. P. Kherani, and R. Zhu, *Rev. Sci. Instrum.* **86**, 033901 (2015).

<sup>11</sup>A. Melnikov, A. Mandelis, J. Tolev, P. Chen, and S. Huq, *J. Appl. Phys.* **107**, 114513 (2010).

<sup>12</sup>Q. M. Sun, A. Melnikov, and A. Mandelis, *Appl. Phys. Lett.* **101**, 242107 (2012).

<sup>13</sup>J. Y. Liu, A. Melnikov, and A. Mandelis, *J. Appl. Phys.* **114**, 104509 (2013).

<sup>14</sup>J. Y. Liu, A. Melnikov, and A. Mandelis, *Phys. Status Solidi A* **210**, 2135 (2013).

<sup>15</sup>A. Mandelis and A. Melnikov, “Method and apparatus for performing heterodyne lock-in imaging and quantitative non-contact measurements of electrical properties,” U.S. patent 9,131,170 (8 September 2015).

- <sup>16</sup>Q. M. Sun, A. Melnikov, and A. Mandelis, *Phys. Status Solidi A* **213**, 405 (2016).
- <sup>17</sup>Q. M. Sun, A. Melnikov, and A. Mandelis, *Int. J. Thermophys.* **37**, 45 (2016).
- <sup>18</sup>E. Yablonovitch, D. L. Allara, C. C. Chang, T. Gmitter, and T. B. Bright, *Phys. Rev. Lett.* **57**, 249 (1986).
- <sup>19</sup>R. A. Sinton and T. Trupke, *Prog. Photovoltaics: Res. Appl.* **20**, 246 (2012).
- <sup>20</sup>J. A. Giesecke and W. Warta, *Appl. Phys. Lett.* **104**, 082103 (2014).
- <sup>21</sup>J. Giesecke, *Quantitative Recombination and Transport Properties in Silicon from Dynamic Luminescence* (Springer, 2014), Chap. 6.
- <sup>22</sup>A. Mandelis, *Diffusion-Wave Fields* (Springer, 2001), Chap. 9.
- <sup>23</sup>See <http://www.apet.co.kr> for Semiconductor Manufacturing Equipment.
- <sup>24</sup>Q. Wang and B. C. Li, *Int. J. Thermophys.* **37**, 39 (2016).
- <sup>25</sup>A. B. Sproul, M. A. Green, and A. W. Stephens, *J. Appl. Phys.* **72**, 4161 (1992).
- <sup>26</sup>T. Konishi, T. Yao, M. Tajima, H. Ohshima, H. Ito, and T. Hattori, *Jpn. J. Appl. Phys., Part 2* **31**, L1216 (1992).
- <sup>27</sup>B. Lashkari, S. S. S. Choi, M. E. Khosroshahi, E. Dovlo, and A. Mandelis, *Opt. Lett.* **40**, 1145 (2015).
- <sup>28</sup>T. Trupke, R. A. Bardos, M. C. Schubert, and W. Warta, *Appl. Phys. Lett.* **89**, 044107 (2006).
- <sup>29</sup>J. A. Giesecke, R. A. Sinton, M. C. Schubert, S. Riepe, and W. Warta, *IEEE J. Photovoltaics* **3**, 1311 (2013).